SCIENTIFIC REPORTS

OPEN

Seebeck-voltage-triggered self-biased photoelectrochemical water splitting using HfO_x/SiO_x bi-layer protected Si photocathodes

Received: 18 January 2019
Accepted: 12 June 2019
Published online: 24 June 2019

Jin-Young Jung[1], Dae Woong Kim[1], Dong-Hyung Kim[1], Tae Joo Park[1], Ralf B. Wehrspohn[2,3] & Jung-Ho Lee[1]

The use of a photoelectrochemical device is an efficient method of converting solar energy into hydrogen fuel via water splitting reactions. One of the best photoelectrode materials is Si, which absorbs a broad wavelength range of incident light and produces a high photocurrent level (~44 mA·cm^{-2}). However, the maximum photovoltage that can be generated in single-junction Si devices (~0.75V) is much lower than the voltage required for a water splitting reaction (>1.6V). In addition, the Si surface is electrochemically oxidized or reduced when it comes into direct contact with the aqueous electrolyte. Here, we propose the hybridization of the photoelectrochemical device with a thermoelectric device, where the Seebeck voltage generated by the thermal energy triggers the self-biased water splitting reaction without compromising the photocurrent level at 42 mA cm^{-2}. In this hybrid device p-Si, where the surface is protected by HfO_x/SiO_x bilayers, is used as a photocathode. The HfO_x exhibits high corrosion resistance and protection ability, thereby ensuring stability. On applying the Seebeck voltage, the tunneling barrier of HfO_x is placed at a negligible energy level in the electron transfer from Si to the electrolyte, showing charge transfer kinetics independent of the HfO_x thickness. These findings serve as a proof-of-concept of the stable and high-efficiency production of hydrogen fuel by the photoelectrochemical-thermoelectric hybrid devices.

Solar water-splitting systems that directly convert solar energy into storable and transportable hydrogen fuel are a promising approach to sustainably providing cost-effective renewable energy[1–5]. In order to realize self-biased solar water splitting, intensive efforts have been made in the past decades to exploit designed prototype systems including photovoltaic-electrolysis combination cells[6–9], tandem photoelectrochemical (PEC) cells using the dual-semiconductor light absorber[10–14], and colloid-based "Z-scheme" photocatalytic cells[15–25]. These systems are normally better suited to generating an output voltage higher than the sum of thermodynamic potential (1.23 V) and kinetic overpotential (>0.3 V), which is required for a practical water-splitting reaction. However, it compromises the photocurrent level because a tradeoff relationship exists between the photovoltage and photocurrent in systems that operate based on the photovoltaic effect. This fundamental obstacle has limited the solar-to-hydrogen efficiency.

As a new approach to overcoming the aforementioned limitation, recently, the hybridization of the PEC cell with other energy-harvesting devices such as thermoelectric (TE) and piezoelectric generators—which generate an output voltage through the conversion of thermal and mechanical energy resources, respectively—has been proposed[26–28]. In particular, the PEC-TE hybrid device is expected to be a commercially viable approach because it can be operated with absorbed solar energy in the form of photons (using the PEC component) and phonons (using the TE component)[26,29]. The PEC-TE hybrid system—in which the PEC device is electrically connected with the TE device in series—could provide an additional output Seebeck voltage (V_{TE}) as a result of a thermal gradient in the TE in order to overcome the potential barrier required for the water-splitting reaction. In this

[1]Department of Materials and Chemical Engineering, Hanyang University, 55 Hanyangdaehak-ro, Sangnok-gu, Ansan, Kyeonggi-do, 15588, Republic of Korea. [2]Institute of Physics, Martin-Luther-Universität Halle-Wittenberg, Halle, Germany. [3]Fraunhofer Institute for Microstructure of Materials and Systems IMWS Walter-Hülse-Strasse 1, D06120, Halle, Germany. Correspondence and requests for materials should be addressed to T.J. (email: tjp@hanyang.ac.kr) or J.-H.L. (email: jungho@hanyang.ac.kr)

hybrid system, the overall current is determined by the high photocurrent level of the PEC cell (i.e., the TE is only used as a voltage booster). This feature of the PEC-TE hybrid system can decouple the tradeoff relation between the voltage and current, thus maximizing the H_2 power generation (P_{Max}).

Various light-absorbing semiconductors including narrow bandgap (Si, InP, and GaAs) and wide bandgap (TiO_x, CuO_x, FeO_x, and $BiVO_x$) materials have been used as photoelectrodes of PEC cell[30]. In the PEC-TE hybrid systems, because the output Seebeck voltage of the TE can further applied to drive the water splitting reaction, the narrow bandgap semiconductors with a higher photocurrent relative to the wide bandgap semiconductors are effective in maximizing the H_2 power generation. Thus, Si with comparatively narrow bandgap (1.1 eV) is capable of generating a high photocurrent of ~44 $mA{\cdot}cm^{-2}$ via harnessing a large portion of the solar spectrum and is a suitable material as a light-absorbing semiconductor photoelectrode[31]. However, the poor corrosion-resistance of Si is an inherent drawback in terms of the long-term stable operation of the PEC reaction[32]. One suitable strategy for offsetting this drawback is to use a high-atomic-density insulating material as a protective layer that would enable the complete blocking of the electrolyte permeation[33–37]. In general, a high-atomic-density insulator of significant thickness provides excellent protection ability but results in an increase in the transfer resistance of the light-induced charge carriers owing to the tunneling barrier of the insulator[38]. Therefore, for Si PEC devices, it is of paramount importance to design a protection layer that guarantees both long-term stability and facile charge-transfer kinetics.

In this study, we present a PEC-TE hybrid system with a HfO_x/SiO_x bilayer protected Si photocathode to ensure its long-term stability without the deterioration of the charge-transfer kinetics. The PEC-TE hybrid device based on an antireflective Si nanostructure photocathode enables the self-biased PEC water-splitting reaction at a high photocurrent level of ~42 $mA{\cdot}cm^{-2}$, which has a maximum H_2 power generation of 55 $mW{\cdot}cm^{-2}$. The HfO_x, which has strong corrosion resistance in an acidic electrolyte and a relatively higher atomic density (9.68 $g{\cdot}cm^{-3}$) than other dielectric materials such as SiO_x (2.65), AlO_x (3.95), and TiO_x (4.23), physically prevents the permeation of the electrolyte into the Si surface, thereby resulting in long-term stable PEC operation for 200 h. Moreover, on applying V_{TE}, the electrical tunneling barrier of HfO_x becomes irrelevant to the charge transport because the potential drop caused by the application of V_{TE} mainly occurs in the SiO_x layer, which induces the tunneling barrier of HfO_x to be located at a level lower than the conduction band of Si. Therefore, V_{TE} is not only applicable for driving a water-splitting reaction but also for reducing the kinetic overpotential required for charge transfer.

Results

H-terminated and SiO_x-grown p-Si (100) wafers were prepared through the treatment of diluted hydrofluoric acid and hot-water-oxidation, respectively, and these wafers were deposited with an amorphous HfO_x thin film using the atomic layer deposition (ALD) process[39–41]. The chemical composition of HfO_x was confirmed using energy-dispersive X-ray spectroscope (EDXS) mapping and X-ray photoelectron spectroscopy (XPS) spectra (See Supplementary Figs 1 and 2). Figure 1a,b show the high-resolution transmission electron microscope (HRTEM) images for the ALD HfO_x thin film deposited on the H-terminated and SiO_x-grown Si wafers. The HfO_x deposited on H-terminated Si was observed to have a 3-nm-thick $HfSiO_x$ interfacial layer, which is caused by a diffusion of the Si atoms during the ALD (see Fig. 1a)[42]. In contrast, the interfacial layer was not found in the SiO_x-grown Si. Figure 1b shows the TEM image for the atomically thin SiO_x interlayer inserted between the HfO_x and Si without the formation of a $HfSiO_x$ layer. This difference is likely due to the bond strength of Si–O (≈190 $kcal{\cdot}mol^{-1}$)[43] being higher than that of Si–H (≈80 $kcal{\cdot}mol^{-1}$)[44]. The stronger Si–O binding formed by SiO_x growth prevents the Si diffusion on the Si surface, thereby creating the HfO_x/SiO_x bilayer without formation of $HfSiO_x$. The chemical quality of the interface between HfO_x and Si is clearly confirmed by the angle-resolved X-ray photoelectron spectroscopy (ARXPS) results. For the Si2p XPS spectra at the low incident angle that represents the interface information, the H-terminated Si wafer has one dominant state of Si^{3+} originating from the $HfSiO_x$ interfacial layer (Fig. 1c), whereas the SiO_x-grown Si wafer has various sub-oxide states of Si^{1+}, Si^{2+}, Si^{3+}, and Si^{4+} (corresponding to Si_2O, SiO, Si_2O_3, and SiO_2, respectively; see Fig. 1d)[45,46].

Linear sweep voltammetry (LSV) responses for the Si photocathodes protected with HfO_x, SiO_x, and HfO_x/SiO_x were obtained in 0.5-M H_2SO_4 to compare the charge transfer kinetics for the PEC water-splitting reaction (Fig. 2a). Two electrode systems consisting of a Si photocathode and Pt anode were used to determine the potential requirement for the self-biased water-splitting reaction. With a thermodynamic potential barrier of 1.23 eV, additional kinetic overpotential is required for the water-splitting reaction. Owing to the sluggish kinetics of the hydrogen evolution reaction (HER) and oxygen evolution reaction (OER), the application of a minimum potential of ~2.8 V vs. Pt is required for realizing a high photocurrent level of 30 $mA{\cdot}cm^{-2}$. The deposition of a 5-nm-thick HfO_x results in an additional overpotential of 1.1 V at 30 $mA{\cdot}cm^{-2}$ owing to the tunneling barrier of HfO_x, and the increase in the thickness to ~9 nm further increases the overpotential by 1.2 V (indicated by blue curves in Fig. 2a). Interestingly, on inserting a thin SiO_x interlayer between the HfO_x and Si (creating a HfO_x/SiO_x bilayer), the additional overpotential is completely reduced regardless of the HfO_x thickness (indicated by the pink curves in Fig. 2a). The same behavior was observed in the dark LSV characteristics for the degenerated doped n-type (n^+-Si) wafer, which is only attributed to the charge transfer kinetics (Supplementary Fig. 3). This result indicates that the insertion of SiO_x makes the charge transport independent of the tunneling barrier of the HfO_x, which is also verified by the electrochemical impedance spectra (Supplementary Fig. 4).

The negligible tunneling barrier can be explained by the effective engineering of an energy band after the insertion of SiO_x under the application of a voltage for driving the PEC water-splitting reaction. When applying potential to the electrolyte/insulator/semiconductor configuration, the electric field can be built up across the insulator, thereby inducing a potential drop at the insulator layers[47]. When the potential is applied across the HfO_x/SiO_x bilayer, the potential drop can be expressed as

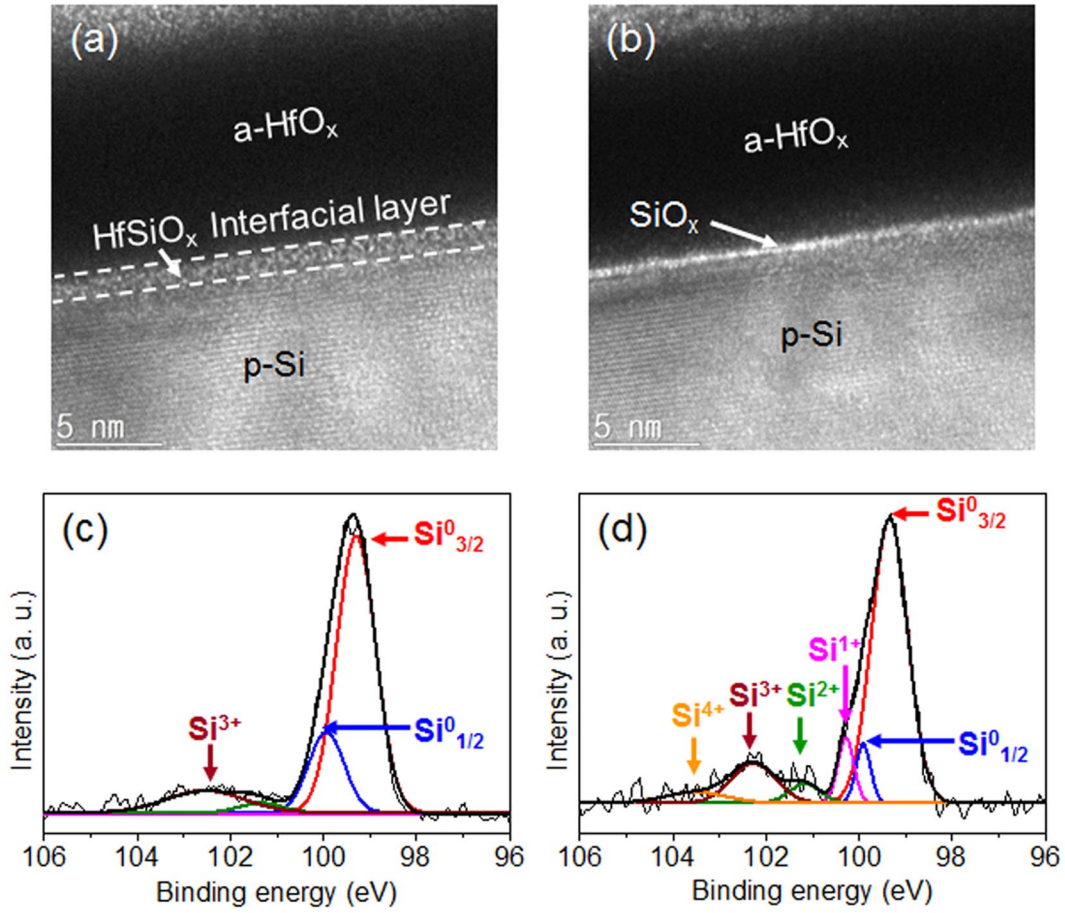

Figure 1. Formation of a-HfO_x/SiO_x bilayer protected p-Si photocathode. TEM images and XPS spectra for the a-HfO_x deposited on (**a**,**c**) H-terminated and (**b**,**d**) SiO_x-grown Si wafers.

$$V_{ox} = E_{SiO_x} t_{SiO_x} + E_{HfO_x} t_{HfO_x} \quad (1)$$

where E and t are the electric field and thickness, respectively. E_{SiOx} and E_{HfOx} are related as

$$E_{HfO_x} = \left(\frac{\varepsilon_{SiO_x}}{\varepsilon_{HfO_x}} \right) E_{SiO_x} \quad (2)$$

The electric field is dominantly applied in the SiO_x layer rather than in HfO_x owing to a dielectric constant of SiO_x (3.9) being much lower than that of HfO_x (11)[47]. This allows a predominant potential drop across the SiO_x layer. The potential drop across the SiO_x layer under the application of potential results in a lying conduction band of HfO_x that is relatively lower than that of Si, as described in Fig. 2b, which shows the band diagram of the HfO_x/SiO_x bilayer. As a result, a tunneling barrier of SiO_x only affects the transport of the charged carrier in the HfO_x/SiO_x bilayer, and consequently, the effective tunneling distance becomes equal to the thickness of the SiO_x monolayer. In contrast, the potential drop for the HfO_x monolayer occurred entirely in the HfO_x monolayer, thus creating a triangular barrier as described in Fig. 2c[48]. Because of the triangular barrier, the tunneling resistance is differentiated with the current density. In the case of a low current level ($<\sim 10\ mA{\cdot}cm^{-2}$), the charge carriers are mostly transferred through the upper region of the triangular barrier in order to minimize the tunneling distance and resistance. Consequently, in the low-current level, the overpotential induced by the tunneling resistance is independent of the thickness. However, in the case of a high photocurrent region ($>\sim 10\ mA{\cdot}cm^{-2}$), charge carriers transfer through all the regions of the barrier and suffer from a large tunneling distance and resistance. Therefore, the overpotential in the high-current level is greatly increased with the thickness.

It is also worth noting that the formation of the $HfSiO_x$ interfacial layer in the HfO_x monolayer induces a hysteresis phenomenon owing to a negative charge trapping/detrapping mechanism at the interfacial layer[49]; the LSV curve is shifted into the anodic direction during the 10 cycles of the LSV scan (see Supplementary Fig. 5). This suggests that the $HfSiO_x$ interfacial layer with a high defect density acts as a recombination site for the charge carrier and also causes an increase in the charge transfer resistance. By contrast, the HfO_x/SiO_x bilayer prevented the formation of $HfSiO_x$ interfacial layer and the hysteresis. To observe the effect of the SiO_x interlayer on the PEC performance of the bilayer protected Si photocathodes, the LSV responses were characterized for the samples with

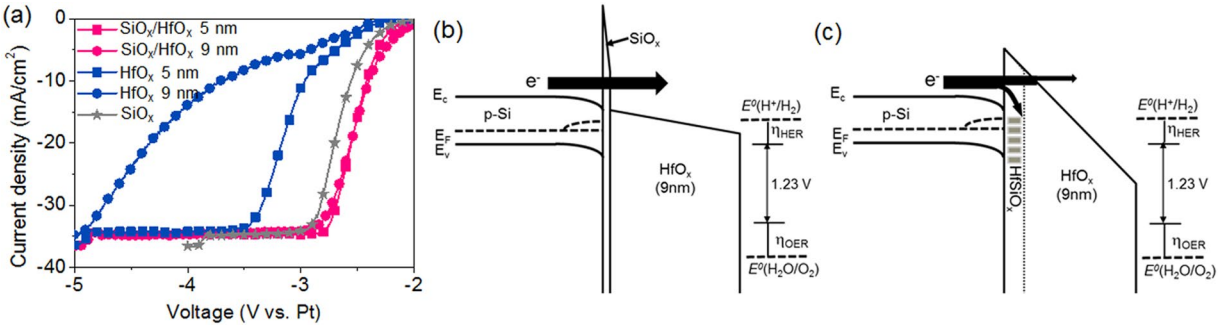

Figure 2. Comparison of PEC performances for p-Si photocathode protected with a-HfO_x monolayer and a-HfO_x/SiO_x bilayer. (**a**) LSV curves of HfO_x monolayer and HfO_x/SiO_x bilayer protected Si photocathodes. Energy band diagrams of (**b**) HfO_x monolayer and (**c**) HfO_x/SiO_x bilayer protected Si photocathodes under application of voltage for the water-splitting reactions.

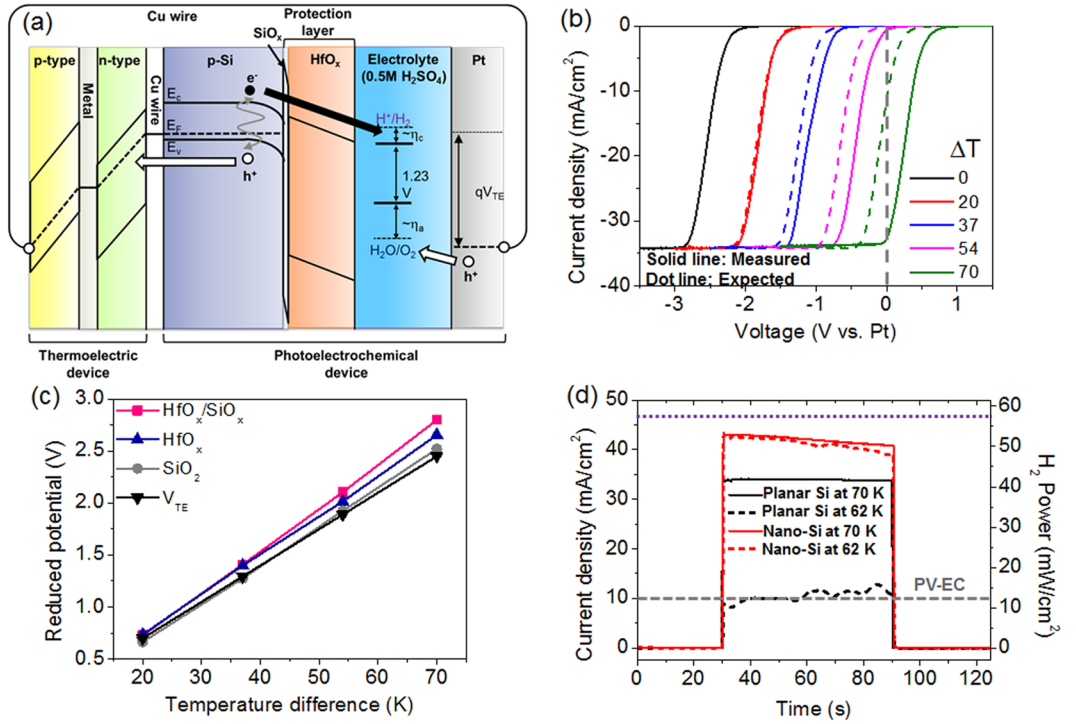

Figure 3. PEC-TE hybrid devices (**a**) Energy band diagram of PEC-TE hybrid device for Seebeck-voltage-driven PEC water-splitting reaction. (**b**) LSV curves of the HfO_x/SiO_x bilayer protected Si photocathode under application of Seebeck voltage as a function of temperature difference (ΔT). (**c**) Plots indicating ΔT-dependent reduced potential for PEC water-splitting reaction; Si photocathodes protected by various insulator layers. (**d**) Photocurrent and P_{max} for PEC-TE device using planar Si and nanostructured Si (nano-Si) at ΔT of 62 K and 70 K. The grey line indicates the P_{max} for the photovoltaic-electrolysis (PV-EC) device[8].

the wet-chemically-grown SiO_x interlayer with oxidation times of 10 min (thin-SiO_x) and 30 min (thick-SiO_x) and with a thermally grown 1.8-nm-thick SiO_2 interlayer (Supplementary Fig. 6). A wet-chemically-grown thin-SiO_x shows the lowest overpotential as compared to the thicker one and the thermally grown SiO_2 interlayer.

The engineering of the HfO_x barrier height under the application of a voltage gives a further advantage in the PEC-TE hybrid system based on the HfO_x/SiO_x bilayer protected Si photocathode. As demonstrated in previous works, a hybrid system in which a PEC device is electrically combined in series with a TE device could promote a self-biased solar water-splitting reaction. The Seebeck voltage generated in the TE device owing to the thermal gradient (V_{TE}) causes the Fermi level of the counter electrodes to be lower than the oxygen evolution level, as depicted in Fig. 3a. This can effectively offset the potential required for driving the self-biased water-splitting reaction while the overall current is determined by the photocurrent of the PEC cell (i.e., the TE is only used as a voltage source)[26]. This was proven by the LSV responses with the driven V_{TE}; the LSV curve for the bare Si photocathode (with DHF treatments) was shifted in the anodic direction in proportion to the applied V_{TE} (see

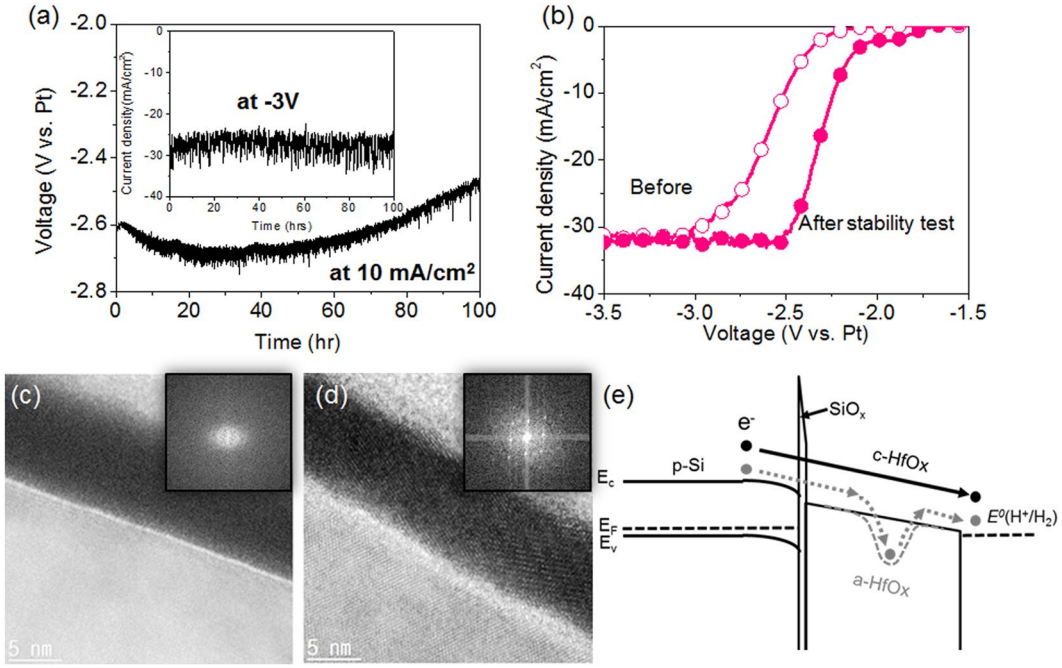

Figure 4. Stability test of HfO_x/SiO_x bilayer protected Si photocathode. (**a**) Measurements of chronopotentiometry at 10 mA cm^{-2} and chronoamperometry at −3 V (inset). (**b**) LSV curves of the Si photocathode before and after the stability test. TEM images of the Si photocathode (**c**) before and (**d**) after the stability test. (**e**) Band diagrams describing the electron transfer kinetics through a-HfO_x and c-HfO_x tunneling layer.

Supplementary Fig. 7). Interestingly, in the case of the HfO_x/SiO_x bilayer protected Si photocathode, an anodic shift degree is larger than the applied V_{TE}, and the overpotential is further reduced by 350 mV at a 70 °C temperature gradient (see Fig. 3b). To clearly differentiate the shifts, the anodic shift degrees of the LSV curve (reducing overpotential) at a photocurrent of 30 mA·cm^{-2} were plotted as a function of ΔT along with the V_{TE} (Fig. 3c). It should be noted that the slope of the linear plot for V_{TE} is the Seebeck coefficient and is represented by the relation $V_{TE} = S\Delta T$. It is apparent that the slop for the HfO_x/SiO_x bilayer protected Si photocathode (41 mV·K^{-1}) is much greater than that for V_{TE} (35 mV·K^{-1}). For the purpose of comparison, we also characterized the slope for the Si photocathodes grown with monolayers of HfO_x and SiO_x (see Supplementary Fig. 8 for the LSV curves). The SiO_x has a slope (36 mV·K^{-1}) that is analogous with that of V_{TE}. In contrast, the slope for the HfO_x is much greater than that for V_{TE} but smaller than that for the HfO_x/SiO_x bilayer. These results are obtained owing to a different tunneling barrier height and potential drop under the applied V_{TE} (see Supplementary Fig. 9 for the band diagrams).

As a result of applying V_{TE}, a saturated photocurrent of 34 mA·cm^{-2} was obtained at a zero potential (i.e., external bias-free). In the PEC-TE hybrid device, an improvement in the photocurrent level is directly correlated with the solar-to-hydrogen conversion efficiency. Thus, we used antireflective Si nanostructures on Si photocathode, which completely absorbed the incident light[50,51] and greatly improved external quantum efficiency (EQE) for the light-induced charge carrier, maximizing the photocurrent of 42 mA·cm^{-2} (see Fig. 3d and Supplementary Figs 10 and 11). While the PEC-TE hybrid system with planar Si provided the maximum H_2 power generation (P_{Max}) of 42 mW·cm^{-2}, the antireflective Si nanostructure photocathode achieved a P_{Max} of 55 mW·cm^{-2}, which is four times greater than that of a photovoltaic-electrolysis combination (P_{Max} of ~12 mW·cm^{-2} indicated by the grey line in Fig. 3d).

The long-term stabilities of the HfO_x/SiO_x bilayer protected Si photocathode were performed using chronoamperometry at a photocurrent level of 10 mA cm^{-2} and using chronopotentiometry at an applied potential of −3 V. Due to the HfO_x thin film which has an (electro)chemical stability in the acidic electrolyte and transparency for all wavelength region of the incident light, the Si photocathode exhibited a stable water-splitting reaction for over 200 h at high photocurrent level of 33 mA/cm^2 (Fig. 4a). The stability achieved at high photocurrent by HfO_x thin film is the best result compared to other metal oxide thin films (see Supplementary Table 1). TiO_x thin films chemically stable in the acidic and alkaline electrolytes have been widely used as a protection layer and have demonstrated long-term stability over 960 hr[52]. However, it has been recently reported ultraviolet (UV) light absorbed in TiO_x causes the electrochemical reduction of TiO_x[53]. Because of this issue, the TiO_x protected Si photocathode operates reliably only when there is no UV irradiation, resulting in low photocurrent. Under the stable operation, the H_2 evolution was characterized by measuring a volume of the H_2 gas collected under a simulated AM 1.5 G 1-Sun illumination while operating under a certain photocurrent level of 32 mA·cm^{-2} for 50 min (Supplementary Fig. 12). The measured H_2 volumes were corresponded well with the theoretically calculated values at a 100% Faraday efficiency based on the total charge passed. After the PEC operation for 200 h, interestingly, the potential was finally shifted in the anodic direction by 200 mV, which was identified by the

anodic shift of the LSV curve (see Fig. 4b). This was found to be the result of the crystallization of the as-deposited a-HfO_x during the PEC water-splitting reaction as observed in the TEM images and X-ray diffraction (XRD) results (Supplementary Fig. 13) of the HfO_x layer before and after the 200 h stability test (see Fig. 4c,d). Because of a bulk defect state in the a-HfO_x that trapped the charge carrier, a substantial resistance was induced for the charge carrier across the a-HfO_x, as depicted in Fig. 4e. In contrast, the crystallized HfO_x significantly reduced the bulk defect density in the a-HfO_x in order to improve the charge transfer kinetics. The crystallization during the solar water splitting reaction at the room temperature condition is an intriguing phenomenon, as it is known to crystallize a-HfO_x in the monoclinic phase at temperature of 500 °C[54]. This can be attributed to an electroforming phenomenon wherein the transition metal oxide can be reformed under the electrical field[55]. This has been observed in transition-metal-oxide-based solid-state electronic devices. This finding presents a new method of improving the insulator quality used in PEC devices.

Discussion

We have presented the PEC-TE hybrid device using HfO_x/SiO_x bilayer protected the Si photocathode in which the HfO_x thin film has a strong corrosion-resistance against the acidic electrolyte. The application of the Seebeck voltage generated in the TE device to the PEC device not only drove the self-biased solar water-splitting reaction but also promoted the ease of charge transfer through the HfO_x tunneling barrier. On applying the Seeback voltage to the HfO_x/SiO_x bilayer/Si photocathode, the conduction band of HfO_x reached an energy level lower than the conduction band of Si, thereby allowing the electron transfer to become independent of the HfO_x tunneling barrier. Because of the kinetic benefit, the voltage required for the self-biased water-splitting reaction of the Si photocathode is lowered by 0.35 V. As a result, the planar-Si-photocathode-based PEC-TE hybrid realized the self-biased water-splitting reaction with the evolved H_2 power of 40 mW cm^{-2} at a temperature difference of 70 °C. By adopting antireflective Si nanostructures that improve the photocurrent level to 42 mA·cm^{-2}, the stored H_2 power reached ~52 mW·cm^{-2}. The HfO_x thin-film protection ensured long-term stable PEC operation for over 200 h. During the stability test, we observed the phase transformation of HfO_x from the amorphous structure into a crystalline structure, which reduces the bulk defect density and thus the kinetic overpotential for the charge transfer through the HfO_x layer.

Method

Preparation of HfO_x thin-film protected Si photocathodes. A single-crystalline Si wafer with a resistivity of 1–10 Ω cm and degenerately doped n^+-type Si (100) wafer with a resistivity of 0.001–0.002 Ω cm were used to characterize the PEC response and charge transfer kinetics, respectively. Prior to the deposition of HfO_x, the Si wafer was dipped into diluted hydrofluoric acid to form an H-terminated surface while removing the native oxide. For growing the SiO_x thin film on the surface of the Si wafer, the H-terminated Si wafer is oxidized through treatment with hot water at 90 °C for 10–30 min. ALD of the HfO_x thin film was performed for both the H-terminated and SiO_x-grown Si wafers to obtain the HfO_x monolayer and HfO_x/SiO_x bilayer coated Si wafers, respectively. An HfO_x thin film was deposited at 280 °C in a 4-inch traveling-wave type ALD reactor (CN-1 Co.) using Tetrakis (ethylmethylamino) hafnium (TEMAHf) and H_2O precursors with a carrier gas of high purity N_2 (99.999%). The TEMAHf, N_2, and H_2O were sequentially injected for 2.5, 30, and 1.5 s, respectively.

Characterization of HfO_x thin films. A HRTEM (JEOL, JEM-2100F, Japan) equipped with an EDXS operated at an accelerating voltage of 200 kV was used to observe the morphology and elemental composition of the HfO_x-thin-film-coated Si wafers. The thicknesses of the HfO_x and SiO_x thin films were measured using spectroscopic ellipsometry (Sopra GES 5E, fitted to a Tauc–Lorentz function using the Cauchey model). The chemical states of the HfO_x and SiO_x thin films were investigated using ARXPS equipped with a monochromatic Al Kα (1.486 eV) source.

Setup of PEC-TE hybrid devices. The PEC device consists of the Si photocathode and Pt mesh anode for the hydrogen evolution reaction (HER) and oxygen evolution reaction (OER), respectively. The back of the Si photocathode was treated with DHF soaking and subsequent scribing using an In–Ga eutectic alloy (Sigma–Aldrich) to fabricate back contacts with a Cu electrode. PEC-TE hybrid systems were used by electrically connecting the PEC device with a TE device in series; the Si photocathode is connected to an anode of the TE device, and a cathode of the TE device is connected to the Pt anode. TE devices with a Seebeck coefficient of 35 mV·K^{-1} and internal resistances of 2.1 Ω, which are commercially available from Kryotherm (Saint-Petersburg, Russia), were employed.

Characterizations of PEC performances. The PEC properties of the Si photocathodes were measured using a potentiostat (Iviumstat, Eindhoven, Netherlands) with a two-electrode configuration (Si photocathode and Pt mesh anode). The PEC responses were characterized using various methods of LSV, chronopotentiometry, and chronoamperometry in 0.5-M sulfuric acid under a 100-mW·cm^{-2} illumination (Xenon lamp equipped with AM 1.5 G filter) and calibrated by a Si photodiode standard cell (PV Measurements, Inc.). The LSV responses were measured under dark and illuminated conditions at a scan rate of 50 mV·s^{-1}. The stability and H_2 evolution measurements were performed using chronopotentiometry and chronoamperometry. Home-made heating and cooling systems were fabricated to control the temperature and were used for applying a constant temperature difference between the front and back of the TE device. The temperature difference was monitored using K-type thermocouples (Center 306 Data Logger, New Taipei City Taiwan). The quantity of hydrogen evolved at the Si photocathode under illumination and the Seebeck voltage application was measured using the volume displacement method wherein the volume of a water-filled flask changes with the evolution of hydrogen gas. A Pt counter electrode covered with a quartz cylinder and proton exchange membrane was used in order to separately collect hydrogen and oxygen gas. All the PEC-TE hybrid system is shown in Supplementary Fig. 14 as a digital image.

Data Availability

The data supporting the findings of this study are available within the article and its Supplementary Information files. All other relevant source data are available from the corresponding author upon reasonable request.

References

1. Fujishima, A. & Honda, K. Electrochemical photolysis of water at a semiconductor electrode. *Nature* **238**, 37–38 (1972).
2. Grätzel, M. Photoelectrochemical cells. *Nature* **414**, 338–344 (2001).
3. Walter, M. G. *et al*. Solar Water Splitting Cells. *Chem. Rev.* **111**, 5815–5815 (2011).
4. Tachibana, Y., Vayssieres, L. & Durrant, J. R. Artificial photosynthesis for solar water-splitting. *Nat. Photon.* **6**, 511–518 (2012).
5. Kudo, A. & Miseki, Y. Heterogeneous photocatalyst materials for water splitting. *Chem. Soc. Rev.* **38**, 253–278 (2009).
6. Jia, J. *et al*. Solar water splitting by photovoltaic-electrolysis with a solar-to-hydrogen efficiency over 30%. *Nat. Commun.* **7**, 13237 (2016).
7. Cox, C. R., Lee, J. Z., Nocera, D. G. & Buonassisi, T. Ten-percent solar-to-fuel conversion with nonprecious materials. *Proc. Natl. Acad. Sci. USA* **111**, 14057–14061 (2014).
8. Luo, J. *et al*. Water photolysis at 12.3% efficiency via perovskite photovoltaics and earth-abundant catalysts. *Science* **345**, 1593–1596 (2014).
9. Kim, S. *et al*. A highly versatile and adaptable artificial leaf with floatability and planar compact design applicable in various natural environments. *Adv. Mater.* **29**, 1702431 (2017).
10. Reece, S. Y. *et al*. Wireless solar water splitting using silicon-based semiconductors and earth-abundant catalysts. *Science* **334**, 645–648 (2011).
11. Jang, J.-W. *et al*. Enabling unassisted solar water splitting by iron oxide and silicon. *Nat. Commun.* **6**, 7447 (2015).
12. Brillet, J. *et al*. Highly efficient water splitting by a dual-absorber tandem cell. *Nat. Photon.* **6**, 824–828 (2012).
13. Abdi, F. F. *et al*. Efficient solar water splitting by enhanced charge separation in a bismuth vanadate-silicon tandem photoelectrode. *Nat. Commun.* **4**, 2195 (2013).
14. Kempler, P. A., Gonzalez, M. A., Papadantonakis, K. M. & Lewis, N. S. Hydrogen evolution with minimal parasitic light absorption by dense Co–P catalyst films on structured p-Si photocathodes. *ACS Energy Lett.* **3**, 612–617 (2018).
15. Chen, J. Q. *et al*. Recent progress in enhancing solar-to-hydrogen efficiency. *J. Power Sources* **280**, 649–666 (2015).
16. Iwase, A., Ng, Y. H., Ishiguro, Y., Kudo, A. & Amal, R. Reduced grapheme oxide as a solid-state electron mediator in Z-scheme photocatalytic water splitting under visible light. *J. Am. Chem. Soc.* **133**, 11054–11057 (2011).
17. Wang, Q. *et al*. Scalable water splitting on particulate photocatalyst sheets with a solar-to-hydrogen energy conversion efficiency exceeding 1%. *Nat. Mater.* **15**, 611–615 (2016).
18. Liu, J. *et al*. Metal-free efficient photocatalyst for stable visible water splitting via a two-electron pathway. *Science* **347**, 970–974 (2015).
19. Yang, X. *et al*. Interfacial optimization of g-C_3N_4-based Z-scheme heterojunction toward synergistic enhancement of solar-driven photocatalytic oxygen evolution. *Appl. Catal. B Environ.* **244**, 240–249 (2019).
20. Liu, Q., Shen, J., Yang, X., Zhang, T. & Tang, H. 3D reduced graphene oxide aerogel-mediated Z-scheme photocatalytic system for highly efficient solar-driven water oxidation and removal of antibiotics. *Appl. Catal. B Environ.* **232**, 562–573 (2018).
21. Liu, Q. *et al*. Unveiling the origin of boosted photocatalytic hydrogen evolution in simultaneously (S, P, O)-codoped and exfoliated ultrathin g-C_3N_4 nanosheets. *Appl. Catal. B Environ.* **248**, 84–94 (2019).
22. Liu, W., Shen, J., Yang, X., Liu, Q. & Tang, H. Dual Z-scheme g-C_3N_4/Ag_3PO_4/Ag_2MoO_4 ternary composite photocatalyst for solar oxygen evolution from water splitting. *Appl. Surf. Sci.* **456**, 369–378 (2018).
23. Lian, Z. *et al*. Plasmonic silver quantum dots coupled with hierarchical TiO2 nanotube arrays photoelectrodes for efficient visible-light photoelectrocatalytic hydrogen evolution. *Sci. Rep.* **5**, 10461 (2015).
24. Lian, Z. *et al*. Photoelectrocatalytic reduction of CO_2 to methanol over a photosystem II-enhanced Cu foam/Si-nanowire system. *J. Environ. Sci.* **60**, 108–113 (2017).
25. Wang, W., Li, F., Zhang, D., Leung, D. Y. C. & Li, G. Photoelectrocatalytic hydrogen generation and simultaneous degradation of organic pollutant via CdSe/TiO_2 nanotube arrays. *Appl. Surf. Sci.* **362**, 490–497 (2016).
26. Shin, S.-M., Jung, J.-Y., Park, M.-J., Song, J.-W. & Lee, J.-H. Catalyst-free hydrogen evolution of Si photocathode by thermovoltage-driven solar water splitting. *J. Power Sources* **279**, 151–156 (2015).
27. Wei, A. *et al*. Triboelectric nanogenerator driven self-powered photoelectrochemical water splitting based on hematite photoanodes. *ACS Nano* **12**, 8625–8632 (2018).
28. Li, T. *et al*. Boosting photoelectrochemical water splitting by TENG-charged Li-ion battery. *Adv. Energy Mater.* **7**, 1700124 (2017).
29. Park, K.-T. *et al*. Lossless hybridization between photovoltaic and thermoelectric devices. *Sci. Rep.* **3**, 2123 (2013).
30. Kim, J. H., Hansora, D., Sharma, P., Jang, J.-W. & Lee, J. L. Toward practical solar hydrogen production – an artificial photosynthetic leaf-to-farm challenge. *Chem. Soc. Rev.* **48**, 1908–1971 (2019).
31. Sun, K. *et al*. Enabling silicon for solar-fuel production. *Chem. Rev.* **114**, 8662–8719 (2014).
32. Bae, D., Seger, B., Vesborg, P. C., Hansen, O. & Chorkendorff, I. Strategies for stable water splitting via protected photoelectrodes. *Chem. Soc. Rev.* **46**, 1933–1954 (2017).
33. Hu, S. *et al*. Amorphous TiO_2 coatings stabilize Si, GaAs, and GaP photoanodes for efficient water oxidation. *Science* **344**, 1005–1009 (2014).
34. Choi, M. J. *et al*. Long-term durable silicon photocathode protected by a thin Al_2O_3/SiO_x layer for photoelectrochemical hydrogen evolution. *J. Mater. Chem. A* **2**, 2928–2933 (2014).
35. Sun, K. *et al*. Stable solar-driven water oxidation to O_2(g) by Ni-oxide-coated silicon photoanodes. *J. Phys. Chem. Lett.* **6**, 592–598 (2015).
36. Yu, Y. *et al*. Enhanced photoelectrochemical efficiency and stability using a conformal TiO_2 film on a black silicon photoanode. *Nat. Energy* **2**, 17045 (2017).
37. Kast, M. G. *et al*. SnO_2/TiO_2 as a base-stable protective layer and antireflective coating for microtextured buried-junction H_2-evolving Si photocathodes. *ACS Appl. Mater. Inter.* **6**, 22830–22837 (2014).
38. Scheuermann, A. G. *et al*. Design principles for maximizing photovoltage in metal-oxide-protected water-splitting photoanodes. *Nat. Mater.* **15**, 99–105 (2016).
39. Lau, C., Srimani, T., Bishop, M. D., Hills, G. & Shulaker, M. M. Tunable n-type doping of carbon nanotubes through engineered atomic layer deposition HfO_X films. *ACS Nano* **12**, 10924–10931 (2018).
40. Tian, H. *et al*. Cost-effective, transfer-free, flexible resistive random access memory using laser-scribed reduced graphene oxide patterning technology. *Nano Lett.* **14**, 3214–3219 (2014).
41. Carlos, E. Boosting electrical performance of high-κ nanomultilayer dielectrics and electronic devices by combining solution combustion synthesis and UV irradiation. *ACS Appl. Mater. Inter.* **9**, 40428–40437 (2017).
42. Wang, L., Xue, K., Xu, J. B., Huang, A. P. & Chu, P. K. Control of interfacial silicate between HfO_2 and Si by high concentration ozone. *Appl. Phys. Lett.* **88**, 072903 (2006).
43. Seidel, H., Csepregi, L., Heuberger, A. & Baumgartel, H. Anisotropic etching of crystalline silicon in alkaline solutions. I. Orientation dependence and behavior of passivation layers. *J. Electrochem. Soc.* **137**, 3612–3626 (1991).

44. Cicero, R. L., Linford, M. R. & Chidsey, C. E. D. Photoreactivity of unsaturated compounds with hydrogen-terminated silicon(111). *Langmuir* **16**, 5688–5695 (2000).
45. Oniki, Y., Iwazaki, Y., Hasumi, M., Ueno, T. & Kuroiwa, K. HfO_2/Si and HfSiO/Si structures fabricated by oxidation of metal thin films. *Jpn. J. Appl. Phys.* **48**, 05DA01 (2009).
46. Miyata, N., Abe, Y. & Yasuda, T. Effect of interfacial Si oxidation on interface dipoles in HfO_2/Si structures. *J. Phys. D: Appl. Phys.* **46**, 315304 (2013).
47. Chakrabarti, B. *et al*. Investigation of tunneling current in SiO_2/HfO_2 gate stacks for flash memory applications. *IEEE Trans. Electron Devices* **58**, 4189–4195 (2011).
48. Lana-Villarreal, T., Straboni, A., Pichon, L. & Alonso-Vante, N. Photoelectrochemical characterization of p-type silicon electrodes covered with tunnelling. *Thin Solid Films* **515**, 7376–7381 (2007).
49. Shen, J. *et al*. Hysteresis-free HfO_2 film grown by atomic layer deposition at low temperature. *Thin Solid Films* **519**, 7723–7726 (2011).
50. Jung, J.-Y. *et al*. Photoelectrochemical water splitting employing a tapered silicon nanohole array. *J. Mater. Chem. A* **2**, 833–842 (2014).
51. Jung, J.-Y. *et al*. A strong antireflective solar cell prepared by tapering silicon nanowires. *Opt. Express.* **18**, A286–A292 (2010).
52. Bae, D. *et al*. Carrier-selective p- and n-contacts for efficient and stable photocatalytic water reduction. *Catal. Today* **15**, 59–64 (2016).
53. Wang, T. *et al*. Transparent Ta_2O_5 protective layer for stable silicon photocathode under full solar spectrum. *Ind. Eng. Chem. Res.* **58**, 5510–5515 (2019).
54. Park, P. K. & Kang, S. W. Enhancement of dielectric constant in HfO_2 thin films by the addition of Al_2O_3. *Appl. Phys. Lett.* **89**, 192905 (2006).
55. Kim, W. G. *et al*. Dependence of the switching characteristics of resistance random access memory on the type of transition metal oxide: TiO_2, ZrO_2, and HfO_2. *J. Electrochem. Soc.* **158**, H417–H422 (2011).

Acknowledgements

This work was supported by the National Research Foundation of Korea (NRF) grant funded by the Korea government (MSIP) (No. 2017R1A2B3006941), and the International Collaborative Energy Technology R&D Program of the Korea Institute of Energy Technology Evaluation and Planning (KETEP) granted financial resource from the Ministry of Trade, Industry & Energy, Republic of Korea (No. 20168520011370).

Author Contributions

J.-Y.J. and J.-H.L. conceived the idea and designed the experiment and wrote the paper. J.-Y.J., D.W.K. and D.-H.K. performed the experiments. All authors discussed the results.

Additional Information

Supplementary information accompanies this paper at https://doi.org/10.1038/s41598-019-45672-4.

Competing Interests: The authors declare no competing interests.

Publisher's note: Springer Nature remains neutral with regard to jurisdictional claims in published maps and institutional affiliations.

Open Access This article is licensed under a Creative Commons Attribution 4.0 International License, which permits use, sharing, adaptation, distribution and reproduction in any medium or format, as long as you give appropriate credit to the original author(s) and the source, provide a link to the Creative Commons license, and indicate if changes were made. The images or other third party material in this article are included in the article's Creative Commons license, unless indicated otherwise in a credit line to the material. If material is not included in the article's Creative Commons license and your intended use is not permitted by statutory regulation or exceeds the permitted use, you will need to obtain permission directly from the copyright holder. To view a copy of this license, visit http://creativecommons.org/licenses/by/4.0/.

© The Author(s) 2019